

Derivation of Cloud Index from Geostationary Satellites and Application to the Production of Solar Irradiance and Daylight Illuminance Data



***Pierre Ineichen
GAP-E, University of Geneva
Richard Perez
ASRC - SUNYA***

February 1999

Accepted for publication in

"Theoretical and Applied Climatology"

Group of Applied Physics - Energy, University of Geneva, Switzerland

Derivation of Cloud Index from Geostationary Satellites and Application to the Production of Solar Irradiance and Daylight Illuminance Data

Pierre Ineichen, Richard Perez*

With 13 Figures

* State University of New York at Albany, NY, USA

Abstract

We investigate in the present paper the relationship between satellite count, global irradiance and other solar and illumination resource components, bringing a particular attention to low solar elevation situations (below 20°) which are very important in northern latitudes. Our investigation is based on data from two geostationary satellites, METEOSAT and GOES, backed by ground measurements in Switzerland and the northeastern USA.

The study of different clear sky normalizations lead to the conclusion that a linear correlation between the global clearness index and the irradiance (like the heliosat method) would be inaccurate for low solar elevations, and therefore for high latitude regions. We developed a model that directly relates an elevation dependent clearness index to the cloud index. This methodology presents a definite advantage because it can be generalized to address the clearness index of other solar radiation components, besides global irradiance, such as direct irradiance, diffuse illuminance, etc.

The correlations described in this paper were developed on the data from Geneva (in the frame of the EC program "Satellite") and evaluated on two other independent data sets (Albany, USA and Lausanne, Switzerland). Their precisions, on a hourly basis, are respectively 30%, 40% and 60% for the global, diffuse and beam components (90 , 55 and 95 W/m^2). The use of independent data for the derivation and the validation of the models shows that those can be used in a wide range of locations, even if the applicability has to be assessed for very different climates.

1. Introduction

Visible satellite images from geostationary satellites such as METEOSAT or GOES are of high interest in the field of solar radiation and illumination resources. They are continuous in time, and provide a spatial coverage that cannot be achieved by ground networks. It is therefore important to assess the precision of methodologies converting these images into solar radiation resource information.

Each image pixel is a measure of the earth's radiance in the visible channel recorded by the satellite at the pixel location. Once corrected for sensor response, pixel brightness – or satellite count, as we will refer throughout this paper – is, in first approximation, linearly related to global irradiance received at the earth's surface [Tarpley 1979, Cano 1986, Schmetz 1989].

This paper investigates the relationship between satellite count, global irradiance and other solar and illumination resource components (e.g., sky luminance). Actually, if the global radiation component is usually derived from satellite images, the secondary components, such as the beam or diffuse radiation, are evaluated with a second model, and applied on the calculated global radiation. This method, even giving satisfactory results, has the great disadvantage to cumulate the bias and the dispersion of the first model on the final result. We propose to derive the secondary component directly from the satellite count. In addition, the evaluation of the radiation in northern latitudes is biased by the use of parameters like the clearness index or clear sky index. These indices are solar elevation dependent and therefore, a linear relation between the cloud index and the clearness index is not realistic for low solar elevations (10° - 20°).

Our investigation is based on data from two geostationary satellites, METEOSAT and GOES-8, backed by ground measurements in Switzerland and the northeastern USA.

2. Experimental Data

Ground Measurements: we used data from Geneva, Switzerland (latitude 46.2° N, longitude 6.1° E, altitude 400m [IDMP-CHE1]) Lausanne, Switzerland (latitude 46.5° N, longitude 6.6° E, altitude 410m

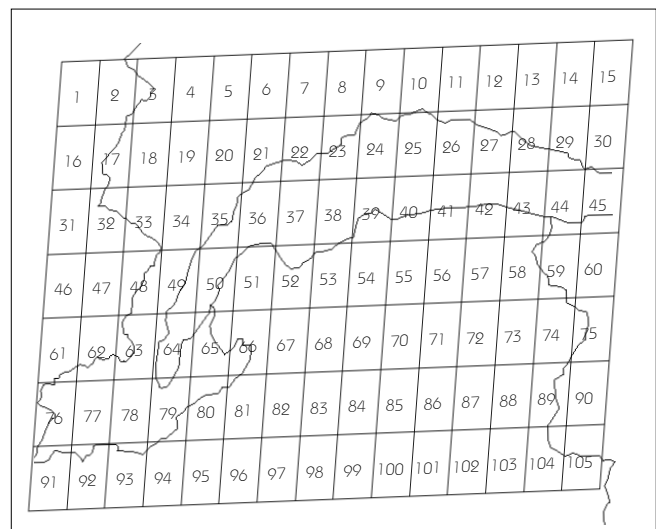


Figure 1. Pixel distribution for the Lake of Geneva region. The station of Geneva is located in pixel #63, and the station of Lausanne in pixel #10. We used pixel #25 as a reference.

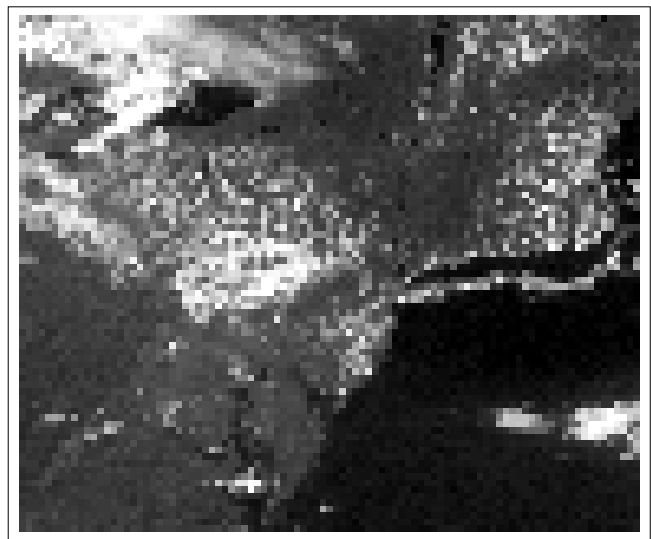


Figure 2. GOES-8 intermediate resolution image covering much of the northeastern United States. The image was taken September 13, 1998 at 13h15 GMT.

[Michel 1997]), and Albany, New York, SA (latitude 42.8°N, longitude 73.8°W, altitude 100m [IDMP-USA2]).

The data from Geneva are 10 minutes' integrals, from April 1994 to March 1995 and are centered on the METEOSAT satellite measurement time. Measurement available in Geneva include global, direct, diffuse irradiance and illuminance, and sky luminance distribution. The data from Lausanne are half-hourly integrals, from April to December 1994, METEOSAT data are within the half-hour corresponding integral. Measurements in Lausanne include only global irradiance. The data from Albany are hourly integrals, from June 1995 to October 1996, the corresponding data are from GOES satellite, and within the hourly integral. Measurements include global, direct and diffuse irradiance.

Geneva and Albany stations include WMO class one and CIE research class instrumentation. Data are subjected to scrupulous visual and automatic quality control [CIE, 1994].

Satellite measurements: the Geneva and Lausanne METEOSAT data cover the Lake of Geneva region as illustrated in Figure 1. Their resolution is currently limited to 8x5.5 km, and are averaged from high resolution images (Hammer 1997).

For Albany, our GOES-8 archive includes intermediate resolution (~10 km) images covering much of the northeastern United States as illustrated in Figure 2. Images are available on an hourly basis and are subsampling extractions from the original images [Unidata, 1995-97].

In this paper, we base our analysis on either the closest pixel to the station, or the 2x2 pixels average containing the station.

3. Cloud index derivation

Most methodologies to retrieve short wave irradiance from satellite images rely on the quasi-linear relationship between atmospheric transmittance and a cloud index parameter linearly dependent on the earth-plus-atmosphere albedo indirectly observed by the satellite as short wave radiance and registered as satellite count [Schmetz 1989, Cano 1986].

The equation that effectively governs all or part of most satellite-to-global irradiance models is:

$$\text{Global irradiance} = G_{\text{clear}} * (1 - n) + G_{\text{min}} \quad (1)$$

where G_{clear} and G_{min} represent the maximum possible and likely minimum irradiances (different expressions of G_{clear} are discussed in section 4), and where n is the cloud index that is effectively defined as [Cano 1986]:

$$n = (C - C_{\text{min}}) / (C_{\text{max}} - C_{\text{min}}) \quad (2)$$

and where C , C_{min} and C_{max} are normalized values of the current, minimum and maximum satellite counts, representing respectively current, clear and heavily overcast conditions.

It is very important that satellite counts be properly normalized so that the cloud index be solely a function of insolation conditions, and not of sun and/or satellite geometric effects.

After correcting the satellite counts for geometric sun-earth distance and for solar incidence, two effects remain: an air mass effect at low solar elevation, and a “hot-spot” effect for low back-scatter angles (sun/satellite angle).

3.1 The air mass effect

When plotting all corrected satellite counts for a given pixel against solar elevation, a familiar pattern emerges with a high and a low boundary representing respectively heavily overcast (bright thick cloud top pixels) and very clear conditions (dark ground pixels). One also notices a sharp increase of the cloud of points for solar elevations below 20°. This increase appears to be most pronounced for the low boundary. An example of such plot is given in Figure 3, first graph, for the pixel covering the station of Geneva (pixel # 63, Figure 1).

In order to quantitatively analyze this effect, we divided the solar elevation abscissa into 60 bins (30 for the station of Lausanne) and looked at the upper and lower boundaries. For each bin, we kept the highest 10% and lowest 10% points, and further rejected the highest and lowest 1% as extreme values. We then obtained an average upper and lower boundary for each bin, surrounded by \pm one standard deviation. The result is shown for Geneva in Figure 3, second graph. The two curves superimposed on these points, and also drawn in the first graph, are linear best fits with respect to the optical air mass am , the ratio of the optical path along the oblique trajectory to the vertical path in the zenith direction (hence they appear curved when plotted as a function of solar elevation).

The trend of the lower boundary (clear skies) may be explained by atmospheric scattering [Lacis 1974, Zelenka 1998]. At low solar elevations, the atmosphere continues to be lit from the side and its diffuse radiation contribution due to Rayleigh and Mie scattering to the clear sky signal received by

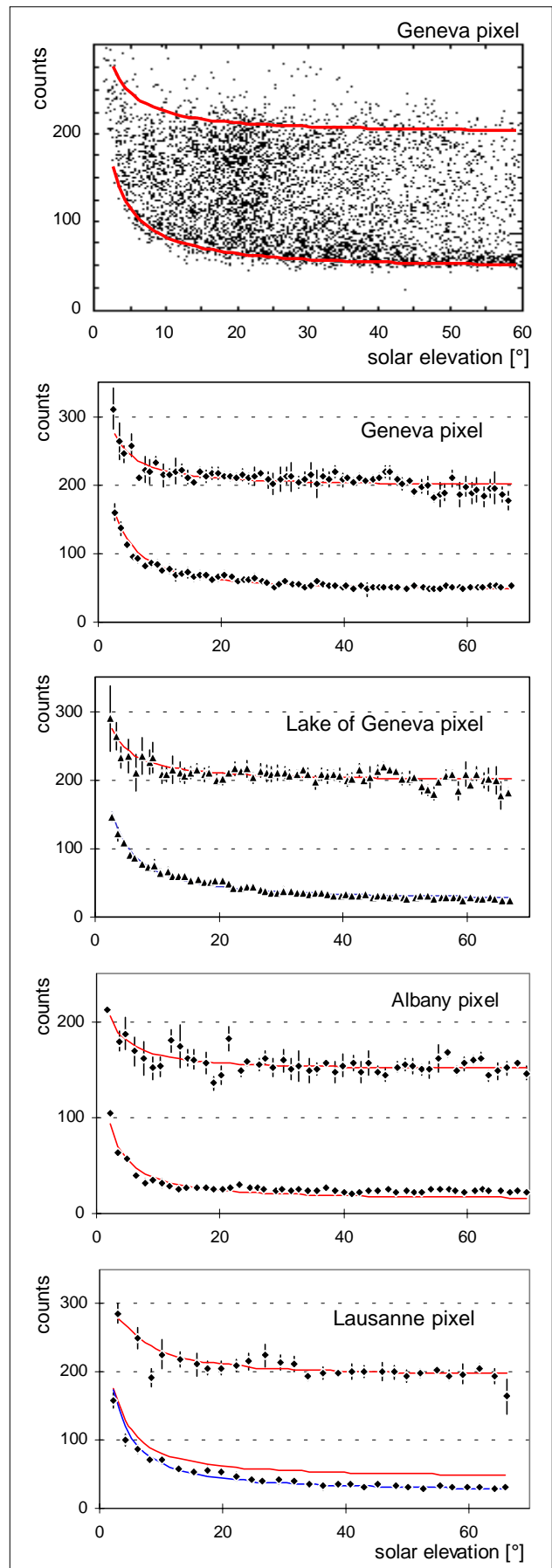


Figure 3. Meteosat and Goes pixel counts against solar elevation. The curves superimposed on the graphs are linear best fits with the optical air mass on the 10% respectively highest and lowest counts.

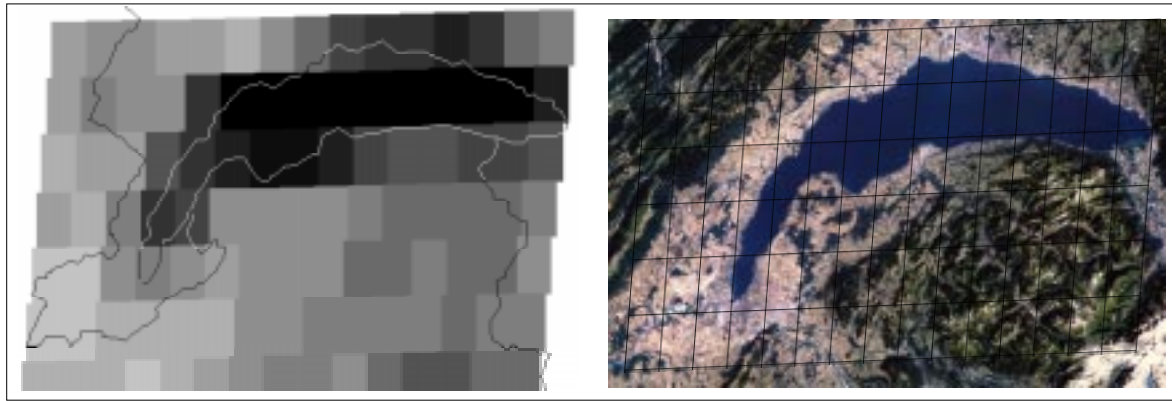


Figure 4. Lowest counts observed in the vicinity of Lake of Geneva (left). The right part is a SPOT satellite photograph of the ground; it illustrates the topography of the same region.

the satellite becomes more important. The earth-reflected signal is superimposed to the Rayleigh contribution. Hence, the cosine-corrected satellite count plotted in Figure 3 increases asymptotically as the solar elevation approaches zero. If the Rayleigh contribution only depends on the geometry, it is not the case of the ground reflected contribution. Therefore, the coefficients of the best fits are specific to the location (the values of the coefficients are given in the appendix).

We observe a similar, but less marked trend at the upper boundary – this boundary represents maximum earth-atmosphere reflectivity, which we assume to be representative of heavily overcast conditions. As these conditions are typically achieved for clouds at relatively low altitudes (2 to 4 km), the atmospheric scattering effect may still be noted above but on a reduced scale.

Similar effects are apparent for two other METEOSAT pixels — Lake of Geneva pixel (# 25) and Lausanne (# 10) – and for the Albany GOES-8 pixel. Note the lower low boundary for the Lake pixel compared to Geneva, due to the lower reflectivity of the water surface. The Lausanne low boundary is between that of the Lake and that of Geneva as this pixel includes both water surface and land. For information, the left part of Figure 4 illustrates the lowest counts (i.e., lowest reflectivity) observed by METEOSAT in the vicinity of Lake of Geneva. The right part of Figure 4 is a SPOT satellite photograph of the ground; it illustrates the topography of the same region. The effect of the dark forests in the right lower edge and the influence of the lake on the contiguous pixels are clearly visible on the lowest METEOSAT counts.

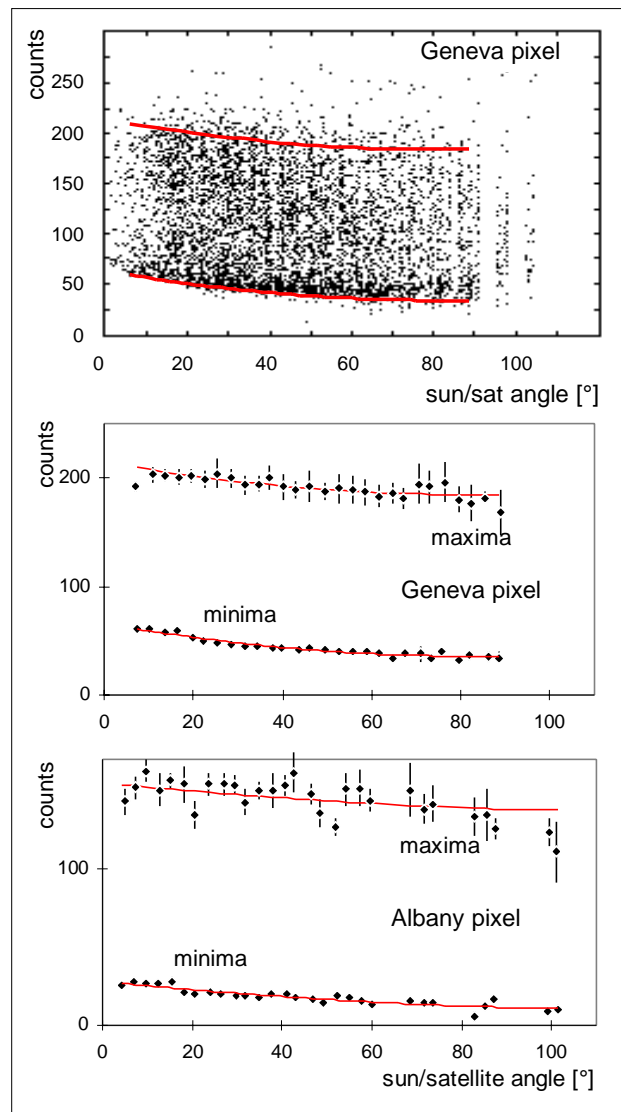


Figure 5. Meteosat and Goes counts against the backscatter angle for Geneva and Albany.

3.2 Backscatter effect

The dependence of the satellite counts with the backscatter angle (the angle between the sun direction and the satellite direction as viewed from the ground) is the second effect that has to be taken into account when deriving the cloud index. Figure 5, first graph, represents the counts for the Geneva pixel versus the backscatter (sun-satellite) angle. In addition to sun-distance, cosine, and sensor correction (GOES' sensor has a quadratic response), the counts plotted in Figure 5 are also corrected for the air mass effect, discussed above. Note that, as the elevation angle of both METEOSAT and GOES with respect to the considered ground points is roughly 40 degrees, the backscatter and air mass effects can be treated independently.

We used the same bin method as above to analyze count variations with sun-satellite angle. Results are given in Figure 5, second and third graphs, for the Geneva and Albany pixels. The data low boundary exhibits a clearly marked trend. As for the previous effect, due to the high dispersion, the data upper limit is difficult to determine precisely. The cloud altitude, type, coverage ratio are highly variable and the «overcast» conditions are not sharply defined. It would appear however that in first approximation, the correction could be applied linearly over the entire counts' scale.

The hot-spot or backscatter effect is a combination of several factors including not only Rayleigh and Mie backscattering on air molecules and aerosols (e.g., Beyer et al., 1996), but also the absence of shadows when the observation and illumination direction, are the same (Pinty, 1991). In Figure 6, we compare the low count boundary for a city and a lake pixel. Both factors affect the city pixel, while only atmospheric backscattering affects the Lake pixel.

3.3 Cloud index

Applying corrections developed in 3.1 and 3.2

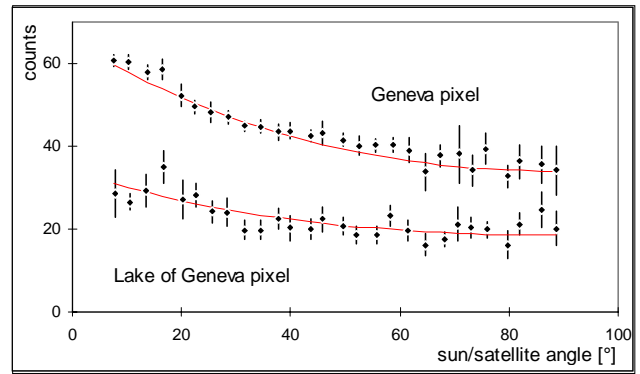


Figure 6. Lower boundary for the two conditions: city and lake.

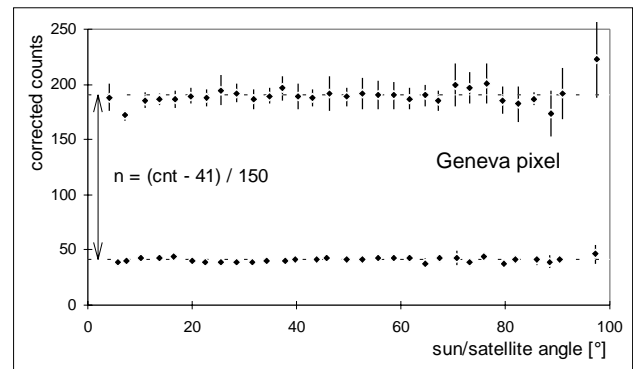


Figure 7. Upper and lower boundary for the corrected counts for the pixel of Geneva (#79).

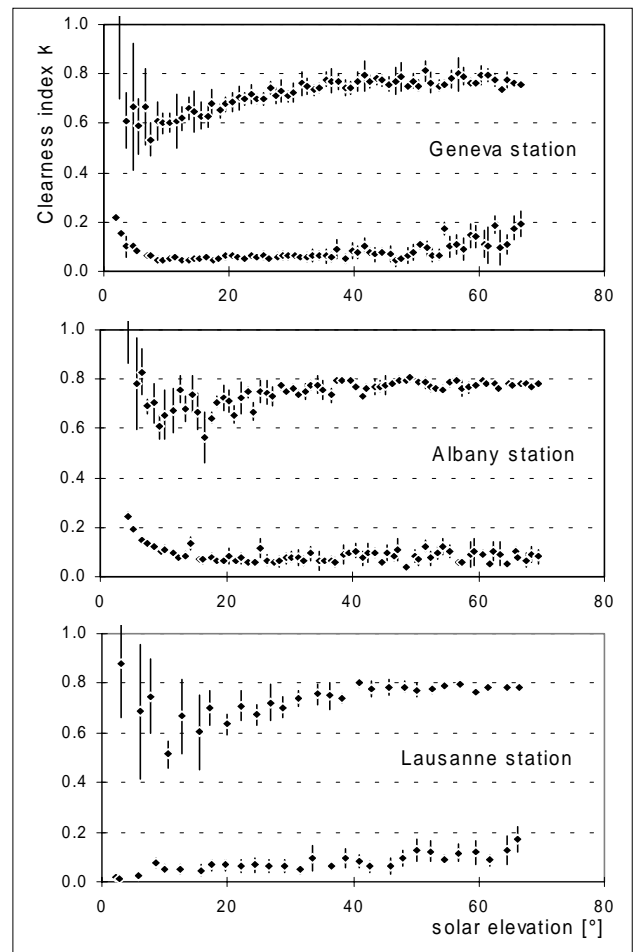


Figure 8. Variation of the clearness index with the solar elevation for Geneva, Albany and Lausanne.

to the satellite counts allows us to produce a sun/satellite-geometry-independent count from which a cloud index, representing solely insolation conditions may be derived. The upper and lower bounds (i.e. C_{\min} and C_{\max} in Equation 2) are presented in Figure 7 for the Geneva pixel. Note that for a given satellite, the upper boundary is observed to be independent from the pixel as should be expected, whereas the lower boundary is dependent on the ground reflectivity.

4. Clear sky normalization

The term G_{clear} in Equation 1, is a critical element of irradiance prediction since it sets highest receivable irradiance at a given site with given local turbidity conditions. As for the cloud index, it is important that the parameters used to determine G_{clear} be solely a function of insolation conditions (i.e. turbidity) without solar geometry distortions.

Using ground-measured irradiance data as experimental evidence, we assess the solar geometry suitability of three simple and commonly used parameterizations: the clearness index K_t , the modified clearness index K_t' and the Kasten's clear sky model.

4.1 The clearness index

The simplest way to normalize the global irradiance is to use the clearness index K_t , which is the global irradiance G_h normalized by the corresponding extra-atmospheric radiation:

$$K_t = G_h / I_o \sin(h) \quad (3)$$

where I_o is the sun-earth distance-corrected solar constant. This clearness index has the disadvantage to depend of the solar elevation angle as shown in Figure 8 from ground measurements in Geneva, Albany and Lausanne. As above, we used a bin method to trace the upper and lower boundary of the data.

Whereas the lower boundary (overcast conditions) does not exhibit notable variation for elevation higher than 10° , the upper boundary (clearest conditions) is highly dependent of the solar elevation. This is because the clearness index fails to account for the increase in direct radiation absorption as a function of air mass.

Hence, K_t is not an ideally suited parameter to set maximum irradiance conditions.

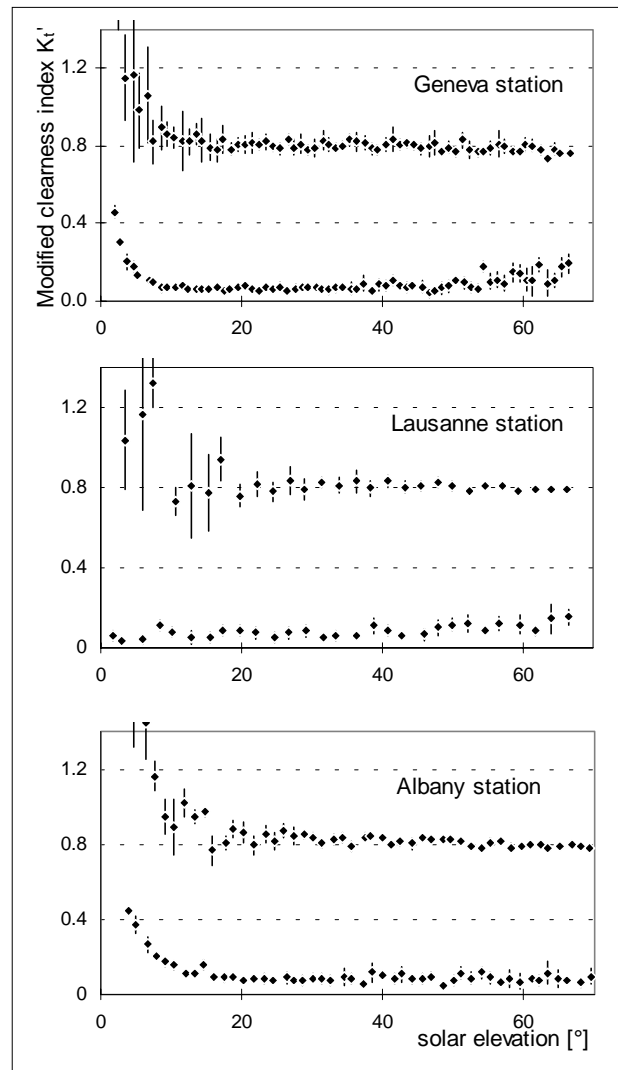


Figure 9. Variation of the modified clearness index with the solar elevation for Geneva, Albany and Lausanne.

4.2 The modified clearness index

This limitation had previously been noted by the authors (Perez, 1990) and a corrected clearness index was proposed:

$$K_t' = K_t / (1.031 \exp(-1.4/(0.9 + 9.4/am)) + 0.1) \quad (4)$$

where am is the optical air mass. Experimentally derived K_t' values are plotted in Figure 9 for Geneva, Lausanne and Albany. For solar elevation higher than 10° , the modified index effectively eliminates solar geometry dependence. However, a reverse trend is clearly visible for low solar elevations. A similar pattern is observed for the two other stations. This pattern is likely caused by the same phenomenon that produces the increase of satellite counts at low solar elevations. For given insolation conditions, the index, corrected for air-mass absorption, still assumes that the cosine law governs maximum irradiance. However, at very low elevations, the atmosphere above receives considerably more radiation than the ground as it is illuminated from its side by the (absorbed) sun and contributes a proportionally higher amount of diffuse to the maximum achievable global irradiance. At sunset, both K_t and K_t' should tend toward infinity since they do not account for this effect.

4.3 The Kasten clear sky

Kasten (1984, Hammer 1997) proposed the following equation to normalize clear sky global radiation. This formulation is used by Beyer (1996):

$$G_{hcK} = 0.84 I_o \sin(h) \cdot \exp(-0.027 am (fh_1 + fh_2 (T_L - 1))) \quad (5)$$

where G_{hcK} represents the global clear sky ground radiation, T_L is the Linke turbidity and fh_1 and fh_2 are coefficients (given in the nomenclature) that relate the altitude of the station with the altitude of the atmospheric interactions (Rayleigh and aerosols).

This formulation, which has been retained by several authors (e.g., Beyer 1996, Zelenka 1998) for relating pixel-derived cloud amounts to global irradiance, has the advantage to be adjusted for local/seasonal prevailing turbidity and site's elevation.

For the present analysis we used monthly Linke Turbidity averages derived from several years

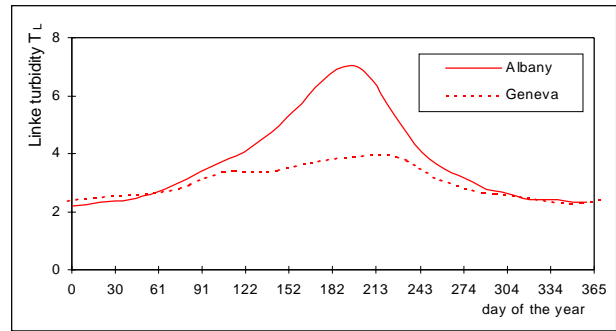


Figure 10. Linke turbidity T_L used in the Kasten clear sky for the station of Geneva and Albany.

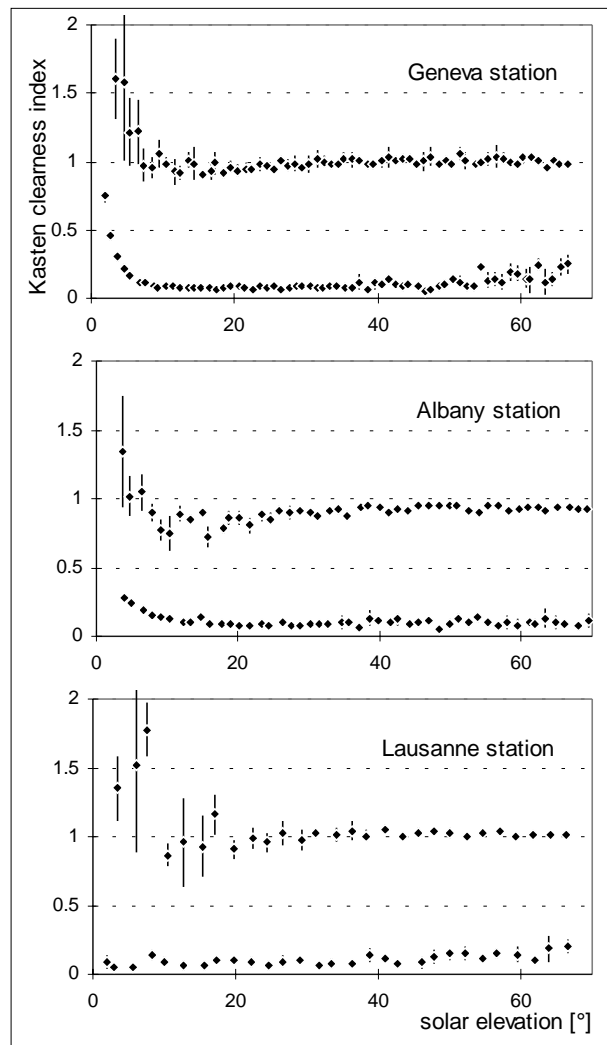


Figure 11. Variation of the Kasten clearness index (G_h/G_{hcK}) with the solar elevation.

of radiation measurements in Albany and Geneva (Figure 10). We then observed the variations of the Kasten clearness index (G_h/G_{hcK}) as a function of solar elevation, deriving the upper and lower bound of data measured in Geneva and Albany (Figure 11). We note that the clear sky model index (upper bound) is roughly independent of solar geometry for elevations above 10° . However, like the above indices, it cannot account for the proportional increase of atmosphere scattered light at very low elevations.

4.4 Applicability of clearness indices

From the above evidence, we conclude that a linear correlation between the global clearness index and irradiance (like the Heliosat method (Diabaté, 1988) or generic formulation (Beyer 1996)) would be inaccurate for solar elevations below 10° , and therefore for high latitude regions.

Two solutions may be envisaged: (1) to define a new clearness index that takes into account the dependence with the solar elevation, and (2) to directly relate an elevation dependent clearness index to the cloud index. The second approach presents a definite advantage because it can be generalized to address the clearness index of other solar radiation components, besides global irradiance (e.g., direct irradiance, diffuse illuminance, etc.). We investigate the viability of this second approach in the following section.

5. Radiation model derivation

In our approach the radiation component (global, diffuse or direct) is normalized by the Kasten clear sky model (section 4.3) and we use the cloud index and solar elevation as input parameters. The derivation of the global radiation is illustrated in Figure 12, where the normalized radiation is represented against the cloud index for 6 different solar elevation categories. For each category, we divided the abscissa into 30 bins and reported the mean value surrounded by \pm one standard deviation. We then made a two parameters regression

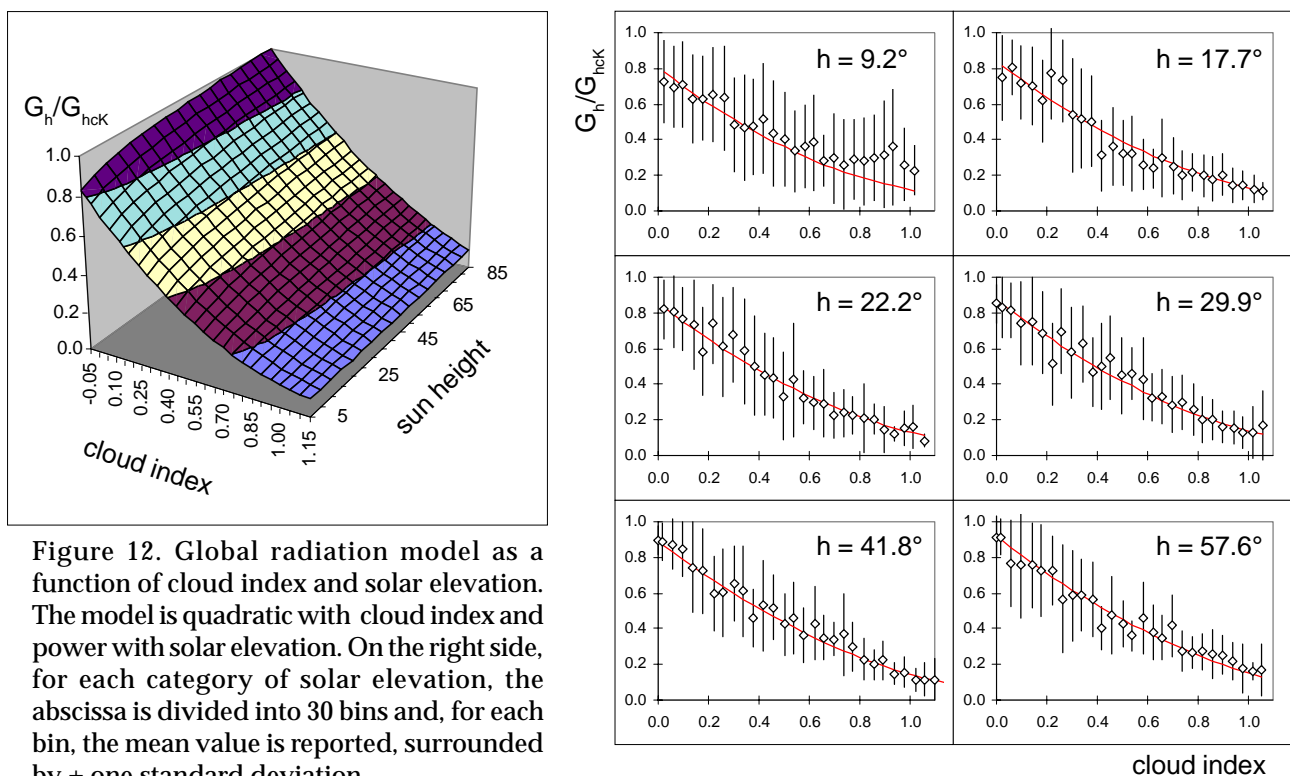
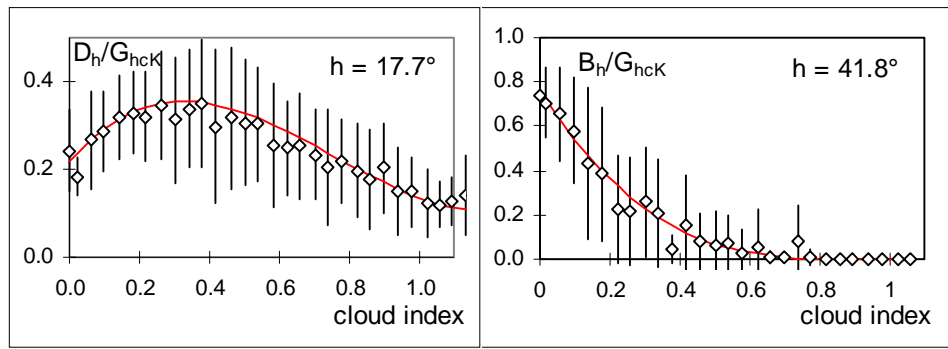


Figure 12. Global radiation model as a function of cloud index and solar elevation. The model is quadratic with cloud index and power with solar elevation. On the right side, for each category of solar elevation, the abscissa is divided into 30 bins and, for each bin, the mean value is reported, surrounded by \pm one standard deviation.

Figure 13. Illustration of the diffuse (left) and beam (right) dependance with cloud index for a given category of solar elevation.



on the weighted points and obtained a quadratic with cloud index and power with solar elevation surface illustrated on Figure 12 (cf. appendix).

The same approach was used to derive the two other radiation components; we used the Kasten clear sky model to normalize the diffuse and the beam radiation and we obtained functions illustrated on Figure 13 for a specific solar elevation bin. We also obtained similar models for the illuminance and luminance components.

The above models are developed on data from Geneva; we then used the two other data banks (Lausanne and Albany) to evaluate independently the obtained regressions. The results are given in the next section.

6. Model precision and results

We made a comparison between calculated and measured values for the three considered data banks. The results are given in Table I. For the majority of the stations, the geographic location is not in the middle of a single pixel and a misalignment is also possible. Therefore, we will do our comparison, as far as possible, using the 2x2 average value of the surrounding pixels' cloud index. The lower boundary is taken constant over the measurement period; it is locally defined as the lower limit of the corrected counts. The results are expressed as a mean bias difference (MBD) between measurements and model (calculation-measurement), and a

		Irradiance					Illuminance				
		mean [W/m ²]	MBD (c-m) [W/m ²] [%]		RMSD [W/m ²] [%]		mean [lux]	MBD (c-m) [lux] [%]		RMSD [lux] [%]	
Geneva	Gh	273	-4	-1%	91	33%	26'952	-327	-1%	8'455	31%
	Dh	130	2	2%	52	40%	14'802	908	6%	5'416	37%
	Bh	143	3	2%	93	65%	11'140	-71	-1%	7'720	69%
	Bn	247	5	2%	168	68%	20'098	-670	-3%	14'859	74%
Lausanne	Gh	329	-12	-4%	97	29%					
Albany	Gh	366	9	2%	95	26%					
	Dh	169	7	4%	64	38%					
	Bh	222	24	11%	119	54%					
	Bn	359	29	8%	202	56%					
Geneva	Lvz					[cd/m ²] 6'281	[cd/m ²] 39	1%	[cd/m ²] 2'951	47%	

Table 1. Comparison between measured and modelled values for different conditions, for the radiation and the illuminance components. The values are expressed as a mean bias difference (MBD) between measurements and model (calculation-measurement), and a root mean square difference (RMSD) giving the fluctuation between the model and the measurements (precision of the model). The mean value of the irradiances, illuminances and luminance are also given.

root mean square difference (RMSD) giving the fluctuation between the model and the measurements (precision of the model).

From Table 1, the following conclusions can be drawn:

- the trends of the results are very similar for the three stations. The global radiation model has a very low bias and a precision of the order of 30% (95 W/m²). The -4% bias for Lausanne is due to the proximity of the Lake,
- the determination of the diffuse and the beam components gives very good results if one keeps in mind that the only input parameter is a reflectance,
- the diffuse radiation component is evaluated with a satisfying bias and a 38-40% precision (55 W/m²),
- the beam component presents a higher bias for the Albany station; it can be explained by the difference in the climate: the average beam radiation is 30% higher in Albany than in Geneva,
- the biases and precisions for the illuminance and irradiance components show very similar trends and the same kind of conclusions can be drawn,
- the direct way to evaluate the beam radiation from the pixel gives slightly better results than the use of the "global-to-direct model" developed by Perez et al. (1992) and applied on the derived global . A complete comparison is under evaluation by the authors and will be published in a next paper.

7. Conclusions

Based on experimental visible-channel data from two geostationary satellites and ground measurements from the US and Switzerland, we have presented a pragmatic identification of the secondary solar geometry effects (high air mass and back-scatter) that distort the determination of the cloud index parameter which is at the core of many simple satellite-to-irradiance models.

Further, we have shown that simple clear sky parameterizations used by these simple models did not account for high air mass distortions. This led us to propose a simple semi-empirical modeling approach which also has the advantage of being straightforwardly applicable to other solar and daylight availability parameters besides global irradiance. We have proceeded to an initial development and fully independent evaluation of these models.

The precision obtained is about 30% on the total radiation, 40% on the diffuse radiation and 60% on the beam radiation. The use of independent data banks for the derivation and the validation of the models shows that those can be used in a wide range of locations, even if the applicability has to be assessed for very different climates.

The clearness index (modified or not, Kasten, etc) increases strongly for low solar elevations; this can be attributed to the twilight.

Acknowledgments

This project is funded by the Federal Office of Education and Science in the frame of the

European Communities project *Satellite*. We would like to thank the LESO for the data of Lausanne and the University of Oldenburg for the METEOSAT data.

Nomenclature

C	normalized values of the current satellite count		
C_{\min}	normalized values of the minimum satellite count		
C_{\max}	normalized values of the maximum satellite count		
n	cloud index		
G_h	global horizontal radiation	G_{\min}	maximum possible irradiance
B_n	normal beam radiation	G_{clear}	likely minimum irradiance
D_h	diffuse horizontal radiation	G_{hcK}	Kasten clear sky global radiation
L_{vz}	zenith luminance		
T_L	Linke turbidity coefficient		
I_o	solar constant	am	optical air mass
		h	solar elevation angle
		ζ	backscatter (sun/satellite) angle
K_t	clearness index	K_t'	modified clearness index
K_c	Kasten clearness index (G_h/G_{hcK})		
$fh_1 = \exp(-\text{altitude} / 8000)$		$fh_2 = \exp(-\text{altitude} / 1250)$	

Appendix

Satellite count correction

The following terms have to be added to the sun-earth distance and sun elevation corrected counts (correction according to Diabaté 1988).

For Geneva:

air mass correction	=	$- 8 \cdot am$
bascatter correction	=	$- 61 \cdot \sin^2(\frac{1}{2} \cdot \zeta) + 87 \cdot \sin(\frac{1}{2} \cdot \zeta) - 25$

and for Albany:

air mass correction	=	$- 4 \cdot am$
bascatter correction	=	$- 12 \cdot \sin^2(\frac{1}{2} \cdot \zeta) + 33 \cdot \sin(\frac{1}{2} \cdot \zeta) - 27$

Model formulation

Global radiation:

$$G_h/G_{\text{hcK}} = a + b \cdot sh + (c + d \cdot sh) \cdot n + (e + f \cdot sh) \cdot n^2$$

Diffuse radiation

$$D_h/G_{\text{hcK}} = a + b \cdot sh^{-1} + (c + d \cdot sh + e \cdot sh^2) \cdot n + (f + g \cdot sh) \cdot n^2 + (h + i \cdot sh)^{-1} \cdot n^2$$

Beam radiation

$$B_h / G_{hcK} = a + b \cdot sh + (c + d \cdot sh + e \cdot sh^2) \cdot n + (f + g \cdot sh + h \cdot sh^2) \cdot n^2 + (i + j \cdot sh + k \cdot sh^2) \cdot n^3$$

where:

$sh = \sin (\frac{1}{2} \cdot h)$, and the corresponding coefficients (cf. section 5):

	a	b	c	d	e	f	g	h	i	j	k
Global	0.797	0.317	-1.54	1.85	0.917	-2.25	-	-	-	-	-
Diffuse	0.202	0.00845	0.515	3.69	-4.80	-2.58	1.28	0.433	2.24	-	-
Beam	0.304	1.04	-1.60	2.14	-8.49	2.46	-8.40	18.4	-1.15	5.18	-9.90

References

Beyer H. G., Costanzo C., Heinemann D., 1996: Modification of the Heliosat procedure for irradiance Estimates from Satellite Images. *Solar Energy*, 56, 207-212.

Cano D., Monget J.M., Albuissou M., Guillard H., Regas N., Wald L., 1986. A method for the determination of the global solar radiation from meteorological satellite data. *Solar Energy*, 37, 31-39.

CIE 1994: Guide to Recommended Practice of Daylight Measurement. CIE 108, ISBN 3 900 734 50 X, Vienna, Austria.

Diabaté L., Demarcq H., Michaud-Regas N., Wald L., 1988: Estimating incident solar radiation at the surface from images of the earth transmitted by geostationary satellites. *Int. J. Solar Energy*, 5, 261-278.

Hammer A. 1997. PRE University of Oldenburg, personal communication.

IDMP-CHE1, <http://idmp.entpe.fr/stations/che01/che01.html>

IDMP-USA2, <http://idmp.entpe.fr/stations/usa02/usa02.html>

IDMP, International Daylight Measurements Programm, <http://idmp.entpe.fr/>

Kasten F., 1984: Parametrisierung der Globalstrahlung durch Bedeckungsgrad und Trübungsfaktor. *Annalen der Meteorologie Neue Folge*, 20, 49-50.

Lacis A., Hansen J.E., 1974. A parametrization for the absorption of solar radiation in the earth's atmosphere. *J. Atmos. Sci.*, 31, 118-133.

Michel L., 1997: Personal communication, EPFL - LESO, Lausanne, Switzerland.

Perez R., Ineichen P., Seals R., Zelenka A., 1990: Making Full Use of the Clearness Index for Parametrizing Hourly Insolation Conditions. *Solar Energy* Vol. 45, 2,111-114.

Perez R., Ineichen P., Maxwell E. L., Seals R., Zelenka A., 1992: Dynamic Global-to-Direct Irradiance Conversion Models. *ASHRAE Transactions*, V. 98, 3578-3593.

Pinty B., Verstraete M. M., 1991: Extracting Information on Surface Properties from Bidirectional Reflectance Measurements. *J. Geoph. Res.*, 96, D2, 2865-2874.

Tarpley J. D., 1979: Estimating incident solar radiation at the surface from geostationary satellite data. *Journal of App. Meteor.*, 18, 1172-.

Unidata, Internet Data Distribution System. *UCAR*, Boulder, CO, 1995-97

Schmetz J., 1989. Towards a surface radiation climatology: retrieval of downward irradiances from satellites. *Atm. Res.*, 23, 287-321.

Zelenka A., Perez R., Seals R., Renné D., 1998: Effective Accuracy of Satellite-Derived Hourly Irradiance. Accepted for publication in *Theoretical and Applied Climatology*.